Received January 11, 2018, accepted March 1, 2018, date of publication March 8, 2018, date of current version April 18, 2018.

Digital Object Identifier 10.1109/ACCESS.2018.2813298

Hybrid Sub-Gridded Time-Domain Method for Ground Penetrating Radar Simulations Including Dispersive Materials

XIAO-KUN WEI, (Student Member, IEEE), WEI SHAO, (Member, IEEE), AND XIAO-HUA WANG, (Member, IEEE)

School of Physical Electronics, University of Electronic Science and Technology of China, Chengdu 610054, China

Corresponding author: Wei Shao (weishao@uestc.edu.cn)

This work was supported in part by the National Natural Science Foundation of China under Grant 61471105 and Grant 61331007 and in part by the 973 Project under Grant 613273.

ABSTRACT Based on the explicit finite-difference time-domain (FDTD) and implicit Crank–Nicolson (CN) FDTD methods, this paper presents a hybrid sub-gridded scheme whose time step size depends on the coarse grid size for numerically simulating the 3-D ground penetrating radar (GPR) scenarios in lossy, dispersive, and inhomogeneous soils. The time step size of CN-FDTD is independent of the grid size in the dense grid region due to its unconditional stability. Thus, the whole region can be run with a time step size determined by the coarse grid in an absolutely stable fashion. Moreover, a multi-pole Debye dispersion model, solved with auxiliary differential equations (ADEs) for both FDTD and CN-FDTD, is incorporated to simulate realistic GPR scenarios, including the detection of different objects buried in dispersive soils. In order to reduce the matrix size of the 3-D implicit CN-FDTD method, the domain decomposition technique is originally employed to achieve fast calculation. Several numerical examples of the GPR scenarios are provided to demonstrate the accuracy and efficiency of the hybrid sub-gridded ADE-FDTD method.

INDEX TERMS Auxiliary differential equation (ADE) technique, finite-difference time-domain (FDTD) method, ground penetrating radar (GPR) simulation, unconditional stability.

I. INTRODUCTION

Ground penetrating radar (GPR) systems, in which the source emitting device is connected to the transmitting antenna and the signal processing equipment is connected to the receiving antenna, are widely applied to various aspects [1], [2]. Especially, GPR is an effective and convenient way in detecting the objects such as pipes, cables, land mines and hidden tunnels buried beneath the earth surface [3]. In GPR systems, a time-domain electromagnetic pulse is emitted from the transmitting antenna, and the reflected signals from the buried objects and ground are obtained and post-processed at the receiving antenna. Then, instead of running a time-consuming simulation, we can easily identify the concerned characteristics of the geometry under test by directly matching the received GPR response to a previously computed model. Therefore, electromagnetic simulation is useful in compiling a signal dictionary of reflected time-domain waveforms corresponding to interested GPR scenarios.

The finite-difference time-domain (FDTD) method [4], [5] is usually used for numerical modeling and simulation of microwave metasurfaces [6], electromagnetic radiation [7], [8], nanostructures [9], [10], wireless network and whole-space field diffusion [11], [12], and GPR systems [13]–[17], because it not only provides versatile solutions of Maxwell's equations for dispersive and inhomogeneous materials but also possesses powerful ability of capturing time-domain impulse of GPR systems. However, in order to keep numerical stability in the standard FDTD simulation, the time step size is determined by the minimal grid size in the computational domain due to the Courant-Friedrichs-Lewy (CFL) condition [5]. Usually, fine grid division is required when parts of the geometric features need to be modeled in detail in simulating a GPR system. Thus, the uniform dense grid results in a huge number of unknowns and an extremely small time step size, which largely reduce the calculating efficiency of the standard FDTD method, especially for the multiscale problems.

The sub-gridded scheme, in which fine density grids are located inside coarse host grids to locally refine the mesh at regions requiring high resolution, is an efficient way to

numerically model and simulate the GPR system. In literature, a variety of techniques have been proposed to realize the sub-gridded FDTD method. In [18], the whole region including dense and coarse grids is run by using a common small time step size which is chosen according to the dense grid; in [19] and [20], the dense grid region is run at a small time step size and the coarse grid region is run at a large time step size while time-space interpolations connect the different grids together; dense grids in the sub-gridded region can be run with a large time step size determined by the coarse grid, where the dense grid is stabilized by either the alternating-direction-implicit (ADI) FDTD [21]–[23], by a priori removal of unstable eignmodes of the dense grid [24], or by the filtering of unstable spatial harmonics [25], [26]. However, ADI-FDTD uses two sub-marching procedures at each time-marching step, and its tridiagonal property of the coefficient matrix is always broken when the boundary condition is incorporated into ADI-FDTD. Moreover, as the time step size of the ADI-FDTD increases, the rapidly degraded numerical dispersion will largely compromise its accuracy [27], [28]. Although the two methods presented in [24] and [26] retain the explicit update nature of the standard FDTD, model-order reduction and eigenvalue perturbation require the eigenvalue decomposition of the FDTD matrix, and the accuracy of spatial filtering is largely compromised as the time step size increases when the computational domain contains materials with a high value of relative permittivity. The unconditionally stable Crank-Nicolson (CN) FDTD method [29], in which a full time-marching step is used to discretize the Maxwell's equations, is believed to have high numerical accuracy and quite small numerical velocity anisotropy compared with ADI-FDTD [30], [31]. Therefore, CN-FDTD is suitable for the simulation of multiscale problems.

In this paper, a three-dimensional (3-D) hybrid sub-gridded FDTD method, in which the implicit CN-FDTD is used in the local dense-grid region while the explicit FDTD is used in the global coarse-grid region, is presented for efficient simulation of practical GPR detection scenarios. Notably, in the hybrid sub-gridded scheme, the coarse and dense grids can be easily synchronized without time-consuming temporal extrapolations and interpolations because CN-FDTD can be run at a time step size that is free from the CFL stability condition imposed to the dense grid. Then, a stable and convenient way to communicate information between the dense CN-FDTD region and coarse FDTD region is proposed. By doing so, the total unknowns are reduced largely and a common time step size can be chosen according to the CFL limit of the coarse grid.

In realistic GPR simulations, the propagation, reflection and attenuation of electromagnetic waves can be significantly influenced by the frequency dispersion of the soil materials in a wide frequency range from 50 to 1000 MHz [14]. Therefore, a multi-pole Debye dispersion model [32]–[34] is adopted here and incorporated into both FDTD and CN-FDTD based on a generalized auxiliary differential equation (ADE) technique [35]. The uniaxial anisotropic perfectly matched layer (PML) absorbing boundary condition extended to the dispersive soil regions truncates the computational domain [36], [37]. Moreover, the domain decomposition (DD) technique [38]–[40] is originally introduced to reduce the coefficient matrix size and save calculating time of the 3-D CN-FDTD method. Compared with the numerical results obtained from the standard ADE-FDTD and sub-gridded ADE-FDTD, the results of hybrid sub-gridded ADE-FDTD show its high accuracy and efficiency in solving the computationally challenging GPR problems.

II. THEORIES AND FORMULATIONS

A. NUMERICAL FORMULATIONS FOR MULTI-POLE DEBYE MEDIA

The time-domain Maxwell's equations of a medium with frequency-dependent dielectric permittivity can be written

$$\frac{\partial \boldsymbol{D}|_{\boldsymbol{r},t}}{\partial t} = \nabla \times \boldsymbol{H}|_{\boldsymbol{r},t} - \boldsymbol{J}|_{\boldsymbol{r},t} \tag{1}$$

$$\mu_0 \frac{\partial \boldsymbol{H}|_{\boldsymbol{r},t}}{\partial t} = -\nabla \times \boldsymbol{E}|_{\boldsymbol{r},t} \tag{2}$$

where μ_0 is the magnetic permeability of free space, and $\boldsymbol{J}$ is the excitation current density. The relative dielectric permittivity ε_{r} is employed to connect the electric displacement vector $\boldsymbol{D}$ with the electric field intensity $\boldsymbol{E}$ in frequency domain through

$$\frac{\boldsymbol{D}|_{\boldsymbol{r},\omega}}{\varepsilon_0} = \varepsilon_{\mathrm{r}}|_{\boldsymbol{r},\omega}\, \boldsymbol{E}|_{\boldsymbol{r},\omega} \tag{3}$$

where ε_0 is the electric permittivity of free space. The frequency-dependent relative permittivity function of a P-pole Debye dispersion model is given by

$$\varepsilon_{\mathrm{r}}|_{\boldsymbol{r},\omega} = \varepsilon_\infty + \sum_{p=1}^{P} \frac{(\varepsilon_{\mathrm{s}} - \varepsilon_\infty) A_p}{1 + \mathrm{j}\omega\tau_p} \tag{4}$$

where ε_∞ is the permittivity at infinite frequency, ε_{s} is the static permittivity, A_{p} is the pole amplitude, ω represents the angular frequency, τ_{p} is the relation time, and $\mathrm{j} = \sqrt{-1}$. The dispersion parameters of the soil in (4) with moisture content of 2.5% are assigned to be $\varepsilon_\infty = 3.2$, $\varepsilon_{\mathrm{s}} = 4.2$, $\sigma = 0.397 \times 10^{-3}$ S/m, $A_1 = 0.75$, $A_2 = 0.3$, $\tau_1 = 2.71$ ns and $\tau_2 = 0.108$ ns, and the dispersion parameters of the soil with moisture content of 5.0% are assigned to be $\varepsilon_\infty = 4.15$, $\varepsilon_{\mathrm{s}} = 5.15$, $\sigma = 1.11 \times 10^{-3}$ S/m, $A_1 = 1.8$, $A_2 = 0.6$, $\tau_1 = 3.79$ ns and $\tau_2 = 0.151$ ns. The constitutive parameters of the soil model without dispersion are chosen as $\varepsilon_{\mathrm{r}} = 3.6$ and $\sigma = 2.8 \times 10^{-3}$ S/m for the moisture content of 2.5% and $\varepsilon_{\mathrm{r}} = 4.8$ and $\sigma = 6.5 \times 10^{-3}$ S/m for the moisture content of 5.0%, respectively [14].

The Debye model (4) can be imported into the update equations of unconditionally stable CN-FDTD with the generalized ADE scheme. Inserting (4) into (3), we get

$$\frac{\boldsymbol{D}|_{\boldsymbol{r},\omega}}{\varepsilon_0} = \varepsilon_\infty\, \boldsymbol{E}|_{\boldsymbol{r},\omega} + \sum_{p=1}^{P} \frac{(\varepsilon_{\mathrm{s}} - \varepsilon_\infty) A_p}{1 + \mathrm{j}\omega\tau_p}\, \boldsymbol{E}|_{\boldsymbol{r},\omega}\,. \tag{5}$$

Introducing

$$\sum_{p=1}^{P} \boldsymbol{R}_p\big|_{\boldsymbol{r},\omega} = \mathrm{j}\omega\varepsilon_0 \sum_{p=1}^{P} \frac{(\varepsilon_\mathrm{s}-\varepsilon_\infty)\,A_p}{1+\mathrm{j}\omega\tau_p}\,\boldsymbol{E}|_{\boldsymbol{r},\omega} \tag{6}$$

as an auxiliary variable, we can get

$$\mathrm{j}\omega\frac{\boldsymbol{D}|_{\boldsymbol{r},\omega}}{\varepsilon_0} = \mathrm{j}\omega\varepsilon_\infty\,\boldsymbol{E}|_{\boldsymbol{r},\omega} + \frac{1}{\varepsilon_0}\sum_{p=1}^{P}\boldsymbol{R}|_{\boldsymbol{r},\omega}. \tag{7}$$

From (6), the relationship between the auxiliary variable $\boldsymbol{R}$ and the electric field density $\boldsymbol{E}$ can be derived

$$\mathrm{j}\omega\tau_p\,\boldsymbol{R}_p\big|_{\boldsymbol{r},\omega} + \boldsymbol{R}_p\big|_{\boldsymbol{r},\omega} = \boldsymbol{j}\omega\varepsilon_0\,(\varepsilon_\mathrm{s}-\varepsilon_\infty)\,A_p\,\boldsymbol{E}|_{\boldsymbol{r},\omega}\,. \tag{8}$$

With the relation between frequency domain and time domain ($\mathrm{j}\omega \to \partial/\partial t$), (7) and (8) can be written as

$$\frac{\partial\,\boldsymbol{D}|_{\boldsymbol{r},t}}{\partial t} = \varepsilon_0\varepsilon_\infty\frac{\partial\,\boldsymbol{E}|_{\boldsymbol{r},t}}{\partial t} + \sum_{p=1}^{P}\boldsymbol{R}_p\big|_{\boldsymbol{r},t} \tag{9}$$

$$\tau_p\frac{\partial\,\boldsymbol{R}_p\big|_{\boldsymbol{r},t}}{\partial t} + \boldsymbol{R}_p\big|_{\boldsymbol{r},t} = \varepsilon_0\,(\varepsilon_\mathrm{s}-\varepsilon_\infty)\,A_p\frac{\partial\,\boldsymbol{E}|_{\boldsymbol{r},t}}{\partial t}. \tag{10}$$

The final equation for updating $\boldsymbol{E}$ is obtained by substituting (9) into (1)

$$\frac{\partial\,\boldsymbol{E}|_{\boldsymbol{r},t}}{\partial t} = \frac{1}{\varepsilon_0\varepsilon_\infty}\nabla\times\boldsymbol{H}|_{\boldsymbol{r},t} - \frac{1}{\varepsilon_0\varepsilon_\infty}\sum_{p=1}^{P}\boldsymbol{R}_p\big|_{\boldsymbol{r},t} - \frac{1}{\varepsilon_0\varepsilon_\infty}\,\boldsymbol{J}|_{\boldsymbol{r},t}. \tag{11}$$

Using the central difference scheme for temporal discretization (n is the time step index), (11) and (2) become

$$\begin{aligned}\frac{\boldsymbol{E}|_{\boldsymbol{r}}^{n+1}-\boldsymbol{E}|_{\boldsymbol{r}}^{n}}{\Delta t} &= \frac{1}{\varepsilon_0\varepsilon_\infty}\nabla\times\frac{\boldsymbol{H}|_{\boldsymbol{r}}^{n+1}+\boldsymbol{H}|_{\boldsymbol{r}}^{n}}{2}\\ &\quad-\frac{1}{\varepsilon_0\varepsilon_\infty}\sum_{p=1}^{P}\frac{\boldsymbol{R}_p\big|_{\boldsymbol{r}}^{n+1}+\boldsymbol{R}_p\big|_{\boldsymbol{r}}^{n}}{2}\\ &\quad-\frac{1}{\varepsilon_0\varepsilon_\infty}\frac{\boldsymbol{J}|_{\boldsymbol{r}}^{n+1}+\boldsymbol{J}|_{\boldsymbol{r}}^{n}}{2}\end{aligned} \tag{12}$$

$$\mu_0\frac{\boldsymbol{H}|_{\boldsymbol{r}}^{n+1}-\boldsymbol{H}|_{\boldsymbol{r}}^{n}}{\Delta t} = -\nabla\times\frac{\boldsymbol{E}|_{\boldsymbol{r}}^{n+1}+\boldsymbol{E}|_{\boldsymbol{r}}^{n}}{2}. \tag{13}$$

Similarly, (10) can be discretized as

$$\begin{aligned}\tau_p\frac{\boldsymbol{R}_p\big|_{\boldsymbol{r}}^{n+1}-\boldsymbol{R}_p\big|_{\boldsymbol{r}}^{n}}{\Delta t} + \frac{\boldsymbol{R}_p\big|_{\boldsymbol{r}}^{n+1}+\boldsymbol{R}_p\big|_{\boldsymbol{r}}^{n}}{2}\\ = \varepsilon_0\,(\varepsilon_\mathrm{s}-\varepsilon_\infty)\,A_p\frac{\boldsymbol{E}|_{\boldsymbol{r}}^{n+1}-\boldsymbol{E}|_{\boldsymbol{r}}^{n}}{\Delta t}\end{aligned} \tag{14}$$

which can be used to express the auxiliary variable $\boldsymbol{R}_p$ in terms of the electric field density, (14) and (15) become the update equations for $\boldsymbol{E}$ and $\boldsymbol{H}$ at time step $n+1$, respectively.

Inserting (13) and (14) into (12) with reference to [29], we can obtain the implicit updating equations for the electric field in 3-D CN-FDTD. Rewriting the implicit equations as a matrix form, we get

$$\boldsymbol{A}\boldsymbol{E}_{x,y,z}^{n+1} = \boldsymbol{b}^n + \frac{\boldsymbol{J}^{n+1}+\boldsymbol{J}^n}{2}, \quad n=0,1,2,\cdots \tag{15}$$

where $\boldsymbol{A}$ is the coefficient matrix, and $\boldsymbol{b}$ is the known terms. This completes the ADE implementation of (4) in the CN-FDTD method.

B. IMPLEMENTATIONS OF THE HYBRID SUB-GRIDDED SCHEME AND THE DOMAIN DECOMPOSITION TECHNIQUE

Since the unconditionally stable CN-FDTD is employed to stabilize the dense grid, both the coarse and dense grid regions can be run at the time step size determined by the CFL limit of the coarse grid. Instead of the boundary between coarse and dense grids aligned with the tangential magnetic field [19], in this paper, the tangential electric field is located at the boundary between coarse and dense grids [26], [41]. The coarse electric field E on the boundary is calculated by coarse magnetic field H inside the coarse grid and dense magnetic field h inside the dense grid. However, the implicit updating equations in CN-FDTD results in $n+1$ time step index for both e and h inside the dense grid, while the explicit updating equations in FDTD results in $n+1$ time step index for E and $n+1/2$ time step index for H inside the coarse grid. In order to keep numerical stability in communicating information, the boundary nodes connect the dense CN-FDTD region with the coarse FDTD region based on an additional set of equations to update magnetic fields. Here, the explicit formulation to update the dense h_z inside the dense grid by CN-FDTD is shown as

$$\begin{aligned}&h_z^{n+1}\Big|_{i+\frac{1}{2},j+\frac{1}{2},k}\\ &= \frac{2\varepsilon_0\,\varepsilon_\infty|_{i+\frac{1}{2},j+\frac{1}{2},k} - \Delta t\,\sigma_y|_{i+\frac{1}{2},j+\frac{1}{2},k}}{2\varepsilon_0\,\varepsilon_\infty|_{i+\frac{1}{2},j+\frac{1}{2},k} + \Delta t\,\sigma_y|_{i+\frac{1}{2},j+\frac{1}{2},k}}\,h_z^n\big|_{i+\frac{1}{2},j+\frac{1}{2},k}\\ &\quad+\overline{C_{z1}^H}\Big|_{i+\frac{1}{2},j+\frac{1}{2},k}\,\overline{C_{zy}^E}\Big|_{i+\frac{1}{2},j+\frac{1}{2},k}\\ &\quad\cdot\left(\begin{array}{l}e_x^{n+1}\big|_{i+\frac{1}{2},j+1,k} - e_x^{n+1}\big|_{i+\frac{1}{2},j,k}\\ +\,e_x^{n}\big|_{i+\frac{1}{2},j+1,k} - e_x^{n}\big|_{i+\frac{1}{2},j,k}\end{array}\right)\\ &\quad-\overline{C_{z1}^H}\Big|_{i+\frac{1}{2},j+\frac{1}{2},k}\,\overline{C_{zx}^E}\Big|_{i+\frac{1}{2},j+\frac{1}{2},k}\\ &\quad\cdot\left(\begin{array}{l}e_y^{n+1}\big|_{i+1,j+\frac{1}{2},k} - e_y^{n+1}\big|_{i,j+\frac{1}{2},k}\\ +\,e_y^{n}\big|_{i+1,j+\frac{1}{2},k} - e_y^{n}\big|_{i,j+\frac{1}{2},k}\end{array}\right)\\ &\quad+\left(\overline{C_{z1}^H}\Big|_{i+\frac{1}{2},j+\frac{1}{2},k}\,\overline{C_{zz}^H}\Big|_{i+\frac{1}{2},j+\frac{1}{2},k} - \overline{C_{z2}^H}\Big|_{i+\frac{1}{2},j+\frac{1}{2},k}\right)\\ &\quad\cdot\,b_z^n\big|_{i+\frac{1}{2},j+\frac{1}{2},k}\end{aligned} \tag{16}$$

where the coefficients are defined as

$$\begin{aligned}&\overline{C_{z1}^H}\Big|_{i+\frac{1}{2},j+\frac{1}{2},k}\\ &= \frac{2\varepsilon_0\,\varepsilon_\infty|_{i+\frac{1}{2},j+\frac{1}{2},k} + \Delta t\,\sigma_z|_{i+\frac{1}{2},j+\frac{1}{2},k}}{\mu_0\,\mu_\mathrm{r}|_{i+\frac{1}{2},j+\frac{1}{2},k}\left(2\varepsilon_0\,\varepsilon_\infty|_{i+\frac{1}{2},j+\frac{1}{2},k} + \Delta t\,\sigma_y|_{i+\frac{1}{2},j+\frac{1}{2},k}\right)},\\ &\overline{C_{z2}^H}\Big|_{i+\frac{1}{2},j+\frac{1}{2},k}\\ &= \frac{2\varepsilon_0\,\varepsilon_\infty|_{i+\frac{1}{2},j+\frac{1}{2},k} - \Delta t\,\sigma_z|_{i+\frac{1}{2},j+\frac{1}{2},k}}{\mu_0\,\mu_\mathrm{r}|_{i+\frac{1}{2},j+\frac{1}{2},k}\left(2\varepsilon_0\,\varepsilon_\infty|_{i+\frac{1}{2},j+\frac{1}{2},k} + \Delta t\,\sigma_y|_{i+\frac{1}{2},j+\frac{1}{2},k}\right)},\end{aligned}$$

$$\overline{C_{zz}^{H}}\Big|_{i+\frac{1}{2},j+\frac{1}{2},k} = \frac{2\varepsilon_0\,\varepsilon_\infty|_{i+\frac{1}{2},j+\frac{1}{2},k} - \Delta t\;\sigma_x|_{i+\frac{1}{2},j+\frac{1}{2},k}}{2\varepsilon_0\,\varepsilon_\infty|_{i+\frac{1}{2},j+\frac{1}{2},k} + \Delta t\;\sigma_x|_{i+\frac{1}{2},j+\frac{1}{2},k}},$$

$$\overline{C_{zy}^{E}}\Big|_{i+\frac{1}{2},j+\frac{1}{2},k} = \frac{\Delta t\varepsilon_0\,\varepsilon_\infty|_{i+\frac{1}{2},j+\frac{1}{2},k}}{\Delta y\left(2\varepsilon_0\,\varepsilon_\infty|_{i+\frac{1}{2},j+\frac{1}{2},k} + \Delta t\;\sigma_x|_{i+\frac{1}{2},j+\frac{1}{2},k}\right)}$$

and

$$\overline{C_{zx}^{E}}\Big|_{i+\frac{1}{2},j+\frac{1}{2},k} = \frac{\Delta t\varepsilon_0\,\varepsilon_\infty|_{i+\frac{1}{2},j+\frac{1}{2},k}}{\Delta x\left(2\varepsilon_0\,\varepsilon_\infty|_{i+\frac{1}{2},j+\frac{1}{2},k} + \Delta t\;\sigma_x|_{i+\frac{1}{2},j+\frac{1}{2},k}\right)}.$$

An additional set of update equation of dense h_z modified by (16), which is used to calculate the coarse E_y on the boundary by FDTD, can be written as

$$\begin{aligned} h_z^{n+\frac{1}{2}}\Big|_{i+\frac{1}{2},j+\frac{1}{2},k} &= \frac{2\varepsilon_0\,\varepsilon_\infty|_{i+\frac{1}{2},j+\frac{1}{2},k} - \Delta t\;\sigma_y|_{i+\frac{1}{2},j+\frac{1}{2},k}}{2\varepsilon_0\,\varepsilon_\infty|_{i+\frac{1}{2},j+\frac{1}{2},k} + \Delta t\;\sigma_y|_{i+\frac{1}{2},j+\frac{1}{2},k}}\; h_z^{n-\frac{1}{2}}\Big|_{i+\frac{1}{2},j+\frac{1}{2},k} \\ &\quad + 2\,\overline{C_{z1}^{H}}\Big|_{i+\frac{1}{2},j+\frac{1}{2},k}\;\overline{C_{zy}^{E}}\Big|_{i+\frac{1}{2},j+\frac{1}{2},k} \\ &\quad \cdot\left(e_x^n|_{i+\frac{1}{2},j+1,k} - e_x^n|_{i+\frac{1}{2},j,k}\right) \\ &\quad - 2\,\overline{C_{z1}^{H}}\Big|_{i+\frac{1}{2},j+\frac{1}{2},k}\;\overline{C_{zx}^{E}}\Big|_{i+\frac{1}{2},j+\frac{1}{2},k} \\ &\quad \cdot\left(e_y^n\Big|_{i+1,j+\frac{1}{2},k} - e_y^n\Big|_{i,j+\frac{1}{2},k}\right) \\ &\quad + \left(\overline{C_{z1}^{H}}\Big|_{i+\frac{1}{2},j+\frac{1}{2},k}\;\overline{C_{zz}^{H}}\Big|_{i+\frac{1}{2},j+\frac{1}{2},k} - \overline{C_{z2}^{H}}\Big|_{i+\frac{1}{2},j+\frac{1}{2},k}\right) \\ &\quad \cdot\; b_z^{n-\frac{1}{2}}\Big|_{i+\frac{1}{2},j+\frac{1}{2},k}. \end{aligned} \tag{17}$$

By doing so, the late-time stability can be maintained for the proposed hybrid sub-gridded ADE-FDTD method, which is confirmed by running an extended time simulation for 300000 time-marching steps.

The conformal FDTD technique [42] is employed to accurately model curved metallic and dielectric boundaries, which are often encountered when typical underground targets are modeled. Furthermore, the efficient DD technique [40] is extended to 3-D computational domain to reduce the matrix size and save the calculating time of the implicit CN-FDTD. The whole computational domain is decomposed into some small subdomains, and the solution of the original large system of equations can be reduced to those of small independent subsystems. As for the independence of each subsystem, DD-CN-FDTD is easy to be implemented in a parallel manner.

III. NUMERICAL RESULTS

In this section, two typical GPR scenarios, in which the target to be detected is a cylindrical pipe buried in dispersive soils, are numerically solved by the hybrid sub-gridded ADE-FDTD method. The cylinder is either metallic or dielectric. All calculations in this paper were performed on an Intel (R) Xeon (R) CPU E5-2650 v2 @ 2.60 GHz Workstation with 128 GB RAM.

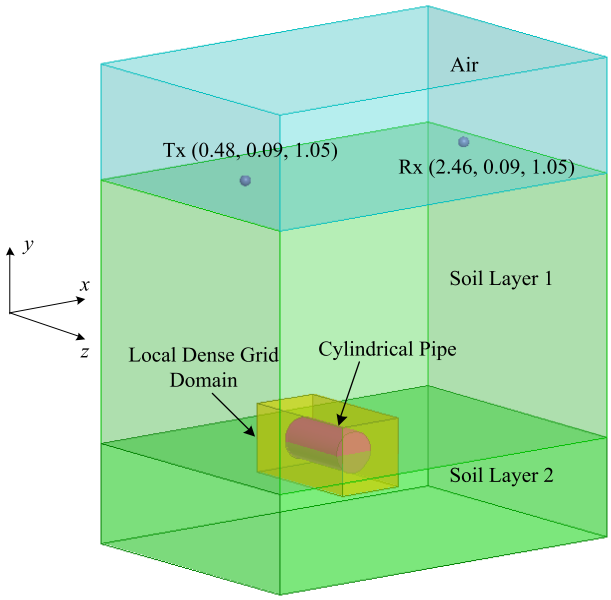

FIGURE 1. 3-D computational region of a typical GPR system with a cylindrical pipe. The Tx and Rx antennas are placed at (0.48 m, 0.09 m, 1.05 m) and (2.46 m, 0.09 m, 1.05 m), respectively, 0.09 m above the soil surface. The diameter and the length of the cylindrical pipe are 0.15 m and 0.30 m, respectively, and its center is located 1.98 m beneath the soil surface.

A. METALLIC CYLINDRICAL PIPE

The time-domain GPR response from a metallic cylindrical pipe buried in the dispersive soil with moisture content of 2.5% is considered. Homogeneous media are considered in this case and the soil parameters come from [14], [43]. The Debye dispersive model of (4) is applied to the hybrid sub-gridded FDTD method with the ADE approach [35]. The uniaxial anisotropic PML [36], [37] consists of ten grids here. As illustrated in Fig. 1, since the emphasis is to model the time-domain wave propagation of a GPR system, both the transmitting (Tx) and receiving (Rx) antennas are chosen as point electric dipoles. And the Tx antenna is excited with the first derivative of the Blackmann-Harris pulse [44]

$$J_z(t) = \begin{cases} -\dfrac{2\pi}{T_s}\displaystyle\sum_{n=0}^{3} a_n n \sin\left(\dfrac{2\pi nt}{T_s}\right), & 0 < t < T_s \\ 0, & \text{elsewise} \end{cases} \tag{18}$$

where the central frequency $f_c = 200$ MHz, the time period $T_s = 1.55/f_c$, and the coefficients are $a_0 = 0.3532$, $a_1 = -0.488$, $a_2 = 0.145$ and $a_3 = -0.0102$.

The computational domain is 3.00 m, 3.60 m and 2.10 m along the x-, y- and z-directions, respectively. In the standard FDTD method, a uniform cubic grid of $\Delta_{\text{dense}} \times \Delta_{\text{dense}} \times \Delta_{\text{dense}}$ Yee cells with $\Delta_{\text{dense}} = 10$ mm is used as a reference solution. In the sub-gridded FDTD methods, the pipe

is discretized by dense grids of $\Delta_{\text{dense}} \times \Delta_{\text{dense}} \times \Delta_{\text{dense}}$, embedded in coarse grids of $\Delta_{\text{coarse}} \times \Delta_{\text{coarse}} \times \Delta_{\text{coarse}}$ with $\Delta_{\text{coarse}} = 30$ mm. The time step size of the standard ADE-FDTD and sub-gridded ADE-FDTD methods is chosen according to the CFL limit of the dense grid. However, with DD-CN-FDTD applied to the sub-gridded region, the hybrid sub-gridded ADE-FDTD scheme is enabled to use a larger time step size from the coarse grid, which is 3 times of that from the CFL limit of the dense grid. Furthermore, to cover the same time interval, both the standard ADE-FDTD and sub-gridded ADE-FDTD need 3000 time-marching steps to complete the simulations, whereas the hybrid sub-gridded ADE-FDTD only includes 1000 time-marching steps.

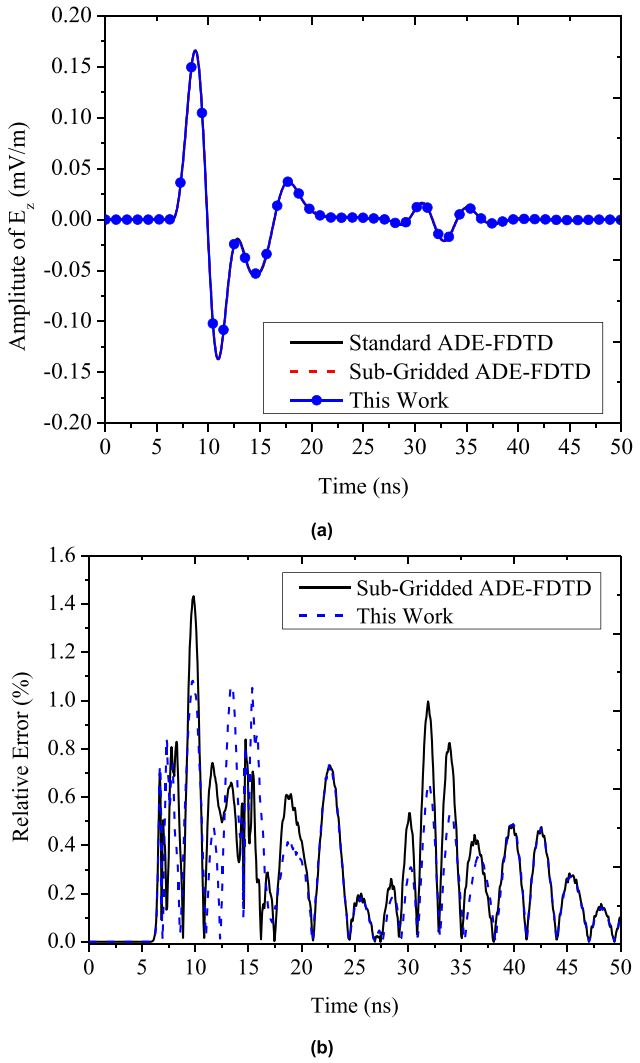

FIGURE 2. Simulation results obtained from three methods. (a) Received amplitude of E_z at the Rx antenna in the GPR system with a metallic cylindrical pipe, calculated by the standard ADE-FDTD, sub-gridded ADE-FDTD and hybrid sub-gridded ADE-FDTD. (b) Relative errors of the sub-gridded ADE-FDTD and hybrid sub-gridded ADE-FDTD.

Fig. 2(a) shows the received amplitudes of E_z at the Rx antenna, obtained with all the three methods. Excellent agreement is clearly observed in Fig. 2(a). To quantify the numerical accuracy, the relative errors of the sub-gridded ADE-FDTD and hybrid sub-gridded ADE-FDTD are given as

$$Error\ (t) = \frac{\left|E_z\ (t) - E_z^{\text{ref}}\ (t)\right|}{\left|E_z^{\text{ref}}\right|_{\max}} \times 100\% \tag{19}$$

where $E_z\ (t)$ is the result from the sub-gridded ADE-FDTD or hybrid sub-gridded ADE-FDTD, $E_z^{\text{ref}}\ (t)$ is the reference solution calculated from the standard ADE-FDTD with an uniform dense grid, and $\left|E_z^{\text{ref}}\right|_{\max}$ is the maximum value of the reference solution over the whole time interval. Fig. 2(b) shows the relative errors and demonstrates that a large time step size has little effect on the numerical accuracy. Furthermore, the time snapshots of the amplitudes of E_z in Fig. 3 confirm the smooth evolution of the scattered fields through the sub-gridded region in which DD-CN-FDTD is operated over the CFL limit of the dense grid.

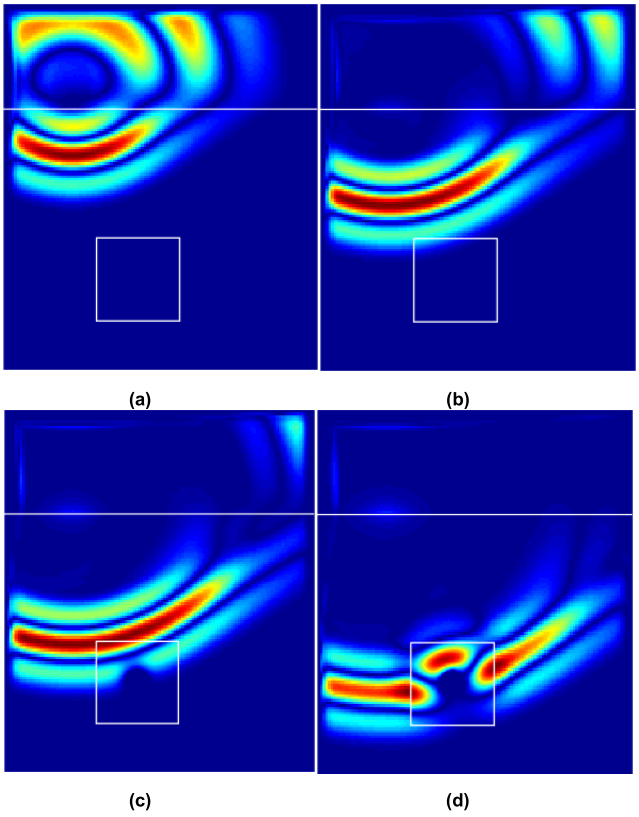

FIGURE 3. Time snapshots of the amplitude of E_z in the computational region with a metallic pipe target, calculated by the hybrid sub-gridded ADE-FDTD method. (a) Snapshot 1. (b) Snapshot 2. (c) Snapshot. (d) Snapshot 4.

The CPU time and memory requirement for the three methods are shown in Table 1, indicating that the CPU time is significantly saved in the hybrid sub-gridded ADE-FDTD scheme. Due to the storage of the sparse coefficient matrices of implicit DD-CN-FDTD, the memory requirement of the hybrid sub-gridded ADE-FDTD is larger than that of the sub-gridded ADE-FDTD, as indicted in Table 1. In fact, it is worth employing the proposed method to save much CPU time at

TABLE 1. CPU time and memory requirement for the three methods.

Method	Time step size (ps)	Number of time-marching steps	CPU time (h)	Memory (GB)
Standard ADE-FDTD	17.33	3000	37.19	27.14
Sub-Gridded ADE-FDTD	17.33	3000	2.20	2.21
This Work	51.99	1000	1.18	4.73

the expense of memory requirement since the hybrid sub-gridded scheme only needs $1/G$ (G is the grid refinement factor) time-marching steps to cover the same time interval of the standard ADE-FDTD and sub-gridded ADE-FDTD.

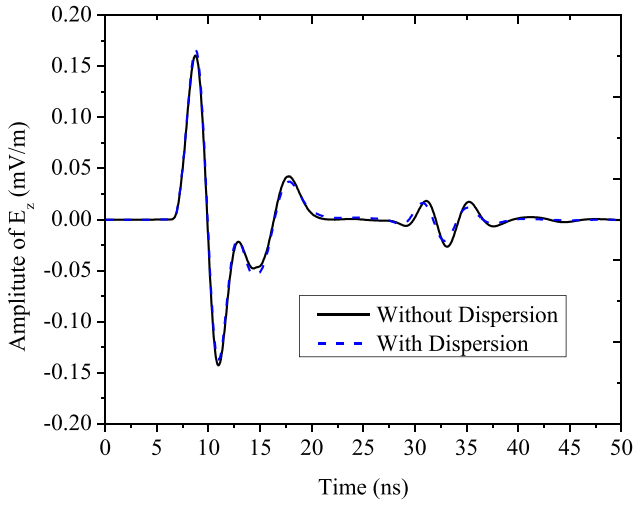

FIGURE 4. Received amplitude of E_z at the Rx antenna in the GPR system with a metallic cylindrical pipe, calculated by the hybrid sub-gridded ADE-FDTD method with and without taking the soil dispersion into consideration.

The reflected waveform from the metallic cylindrical pipe with and without the soil dispersion, obtained from the hybrid sub-gridded ADE-FDTD method, is compared in Fig. 4. It can be found that the received pulse shape can be visibly influenced by the ground dispersion. Moreover, by normalizing to the maximum amplitude, Fig. 5 shows the normalized amplitudes of E_z at the Rx antenna as the Tx-Rx antenna distance is changed from 0 to 2.07 m along the x-direction.

B. DIELECTRIC CYLINDRICAL PIPE

In the second example, the GRP scenario with a target of dielectric cylindrical pipe is considered. In reality, the GPR system is especially useful for the detection of dielectric objects buried in loss, dispersive and inhomogeneous soil. The contrast between the values of permittivity of the target and soil affects the resultant waveforms. In order to illustrate the effects of the relative permittivity of the target, a number of simulations with different relative permittivity values of 9, 25, 49 and 81 are performed in this section. Here, the moisture content of the soil layer 1 is 2.5% and the moisture content of the soil layer 2 is 5.0%, as illustrated in Fig. 1.

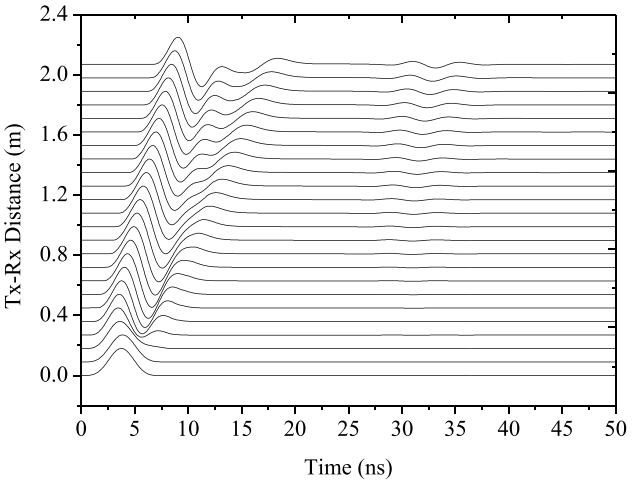

FIGURE 5. Comparison of radar traces for several Tx-Rx antenna distances in the GPR system with a metallic cylindrical pipe.

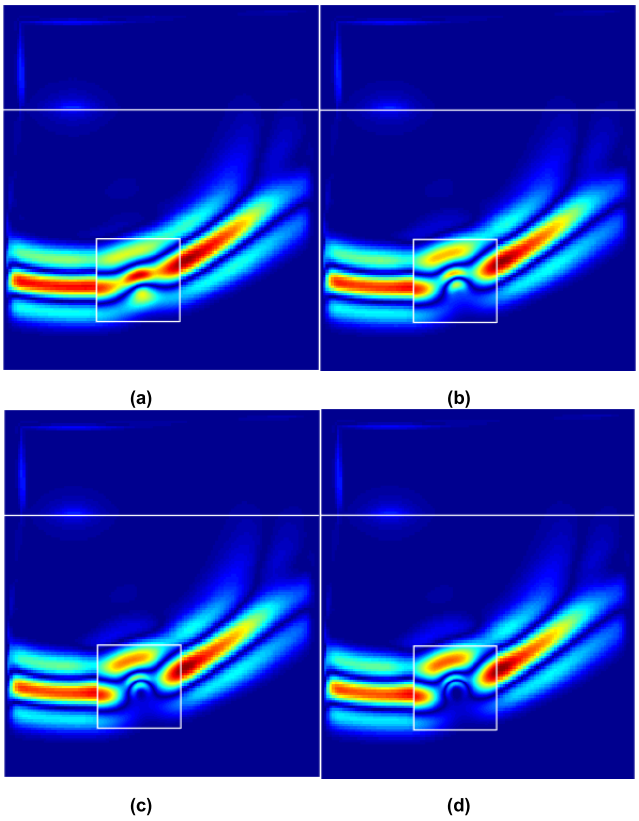

FIGURE 6. Simulation results obtained from two methods with different relative permittivity values of the target. Received amplitude of E_z at the Rx antenna in the GPR system with a target of dielectric cylindrical pipe, calculated by the sub-gridded ADE-FDTD and hybrid sub-gridded ADE-FDTD. (a) Relative permittivity of the target is 9. (b) Relative permittivity of the target is 25. (c) Relative permittivity of the target is 49. (d) Relative permittivity of the target is 81.

In this example, a much finer discretization is required since the target has a high permittivity value and supports small wavelength compared with that of the surrounding soil and air. Therefore, a grid refinement factor of 5 is used

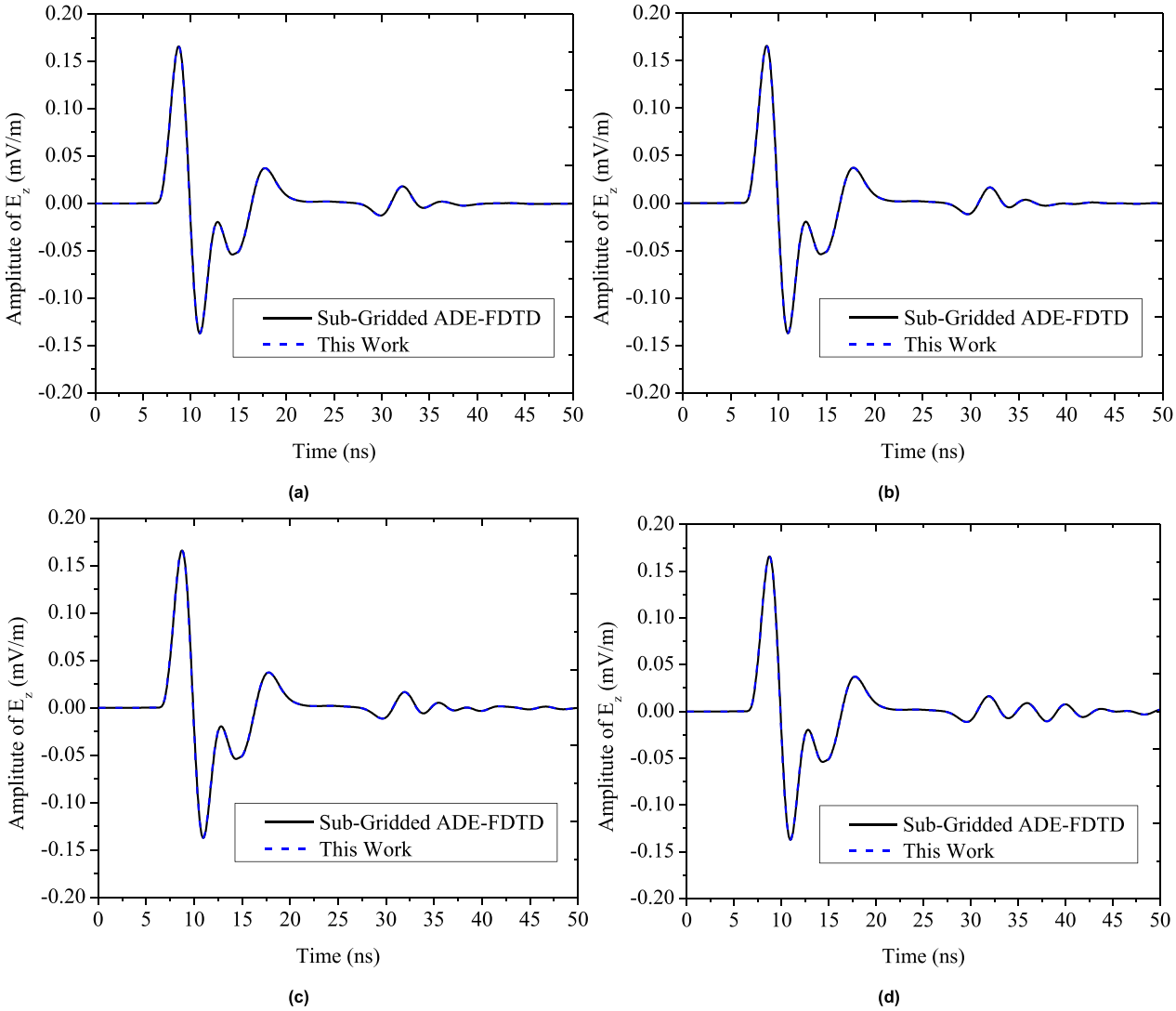

FIGURE 7. Time snapshots of the amplitude of E_z in the computational region with a dielectric pipe target which has different relative permittivity values, calculated by the hybrid sub-gridded ADE-FDTD method. (a) Relative permittivity of the target is 9 and the normalized value of the maximal reflection is 0.21. (b) Relative permittivity of the target is 25 and the normalized value of the maximal reflection is 0.39. (c) Relative permittivity of the target is 49 and the normalized value of the maximal reflection is 0.59. (d) Relative permittivity of the target is 81 and the normalized value of the maximal reflection is 1.00.

in the sub-gridded region. Hence, $\Delta_{\text{coarse}} = 30$ mm and $\Delta_{\text{dense}} = 6$ mm for the sub-gridded ADE-FDTD and hybrid sub-gridded ADE-FDTD. As before, the time step size for the sub-gridded ADE-FDTD is assigned to be the CFL limit of the dense grid, and 5000 time-marching steps are required to simulate the complete time-domain reflection of the dielectric pipe. In the hybrid sub-gridded ADE-FDTD, a time step size determined by the CFL limit of the coarse grid can be used and only 1000 time-marching steps are required to cover the same time interval enabled by the unconditionally stable DD-CN-FDTD. The time step size of the proposed method is 5 times over that of the sub-gridded FDTD. A standard ADE-FDTD simulation with the uniform dense grid of this problem would require too large memory and execution time, and is omitted here.

The received amplitudes of E_z at the Rx antenna, with different relative permittivity values of the target, are shown in Fig. 6. Excellent agreements are observed between the two methods. In Fig. 7, the time snapshots of the amplitude of E_z further confirm the smooth evolution of the scattered fields through the sub-gridded region in which DD-CN-FDTD is operated over the CFL stability limit of the dense grid. Both Figs. 6 and 7 show that the higher relative permittivity value of the target is, the larger reflection is obtained, as expected. The CPU time and memory requirement for the two methods are also given in Table 2, which indicates the largely reduced CPU time by using the hybrid sub-gridded ADE-FDTD. Additionally, Table 2 illustrates again that the time saving is associated with the expense of slightly larger memory requirement than that of the sub-gridded ADE-FDTD.

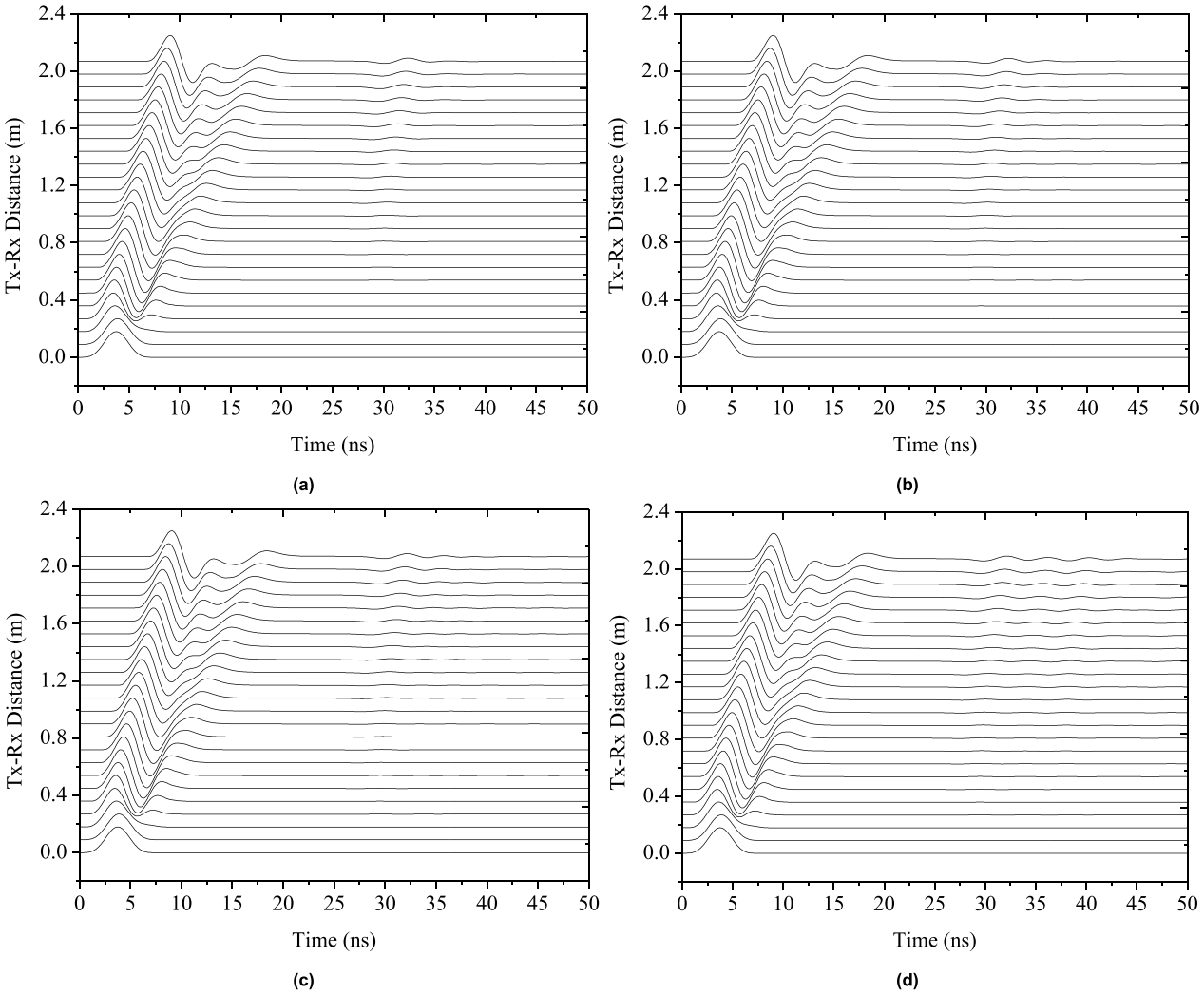

FIGURE 8. Comparison of radar traces for several Tx-Rx antenna distances with different relative permittivity values of the dielectric target. (a) Relative permittivity of the target is 9. (b) Relative permittivity of the target is 25. (c) Relative permittivity of the target is 49. (d) Relative permittivity of the target is 81.

TABLE 2. CPU time and memory requirement for the two methods.

Method	Time step size (ps)	Number of time-marching steps	CPU time (h)	Memory (GB)
Sub-Gridded ADE-FDTD	10.40	5000	3.49	2.35
This Work	51.99	1000	1.47	6.27

Finally, the reflected E_z waveform from the environment and the target with different relative permittivity values at the Rx antenna are shown in Fig. 8. It can be pointed out that the largest reflections are obtained from the dielectric cylindrical pipe with relative permittivity value of 81. The simulation results in this section demonstrate that as the contrast between the soil and the target increases, scattered fields observed at the Rx antenna get larger in amplitude.

IV. CONCLUSION

It is computationally challenging for the standard ADE-FDTD method to numerically model and simulate 3-D realistic GPR scenarios which involve the electromagnetic reflection, diffraction and scattering with multiscale geometries. Fine grid discretization is often required in simulating practical GPR systems either because of their geometrical features which can span several scales of magnitude or because of their high dielectric permittivity and conductivity of the objects and surrounding materials. Sub-gridded ADE-FDTD methods are suitable for this kind of problems, since they can accurately simulate multiscale features. In this paper, a hybrid sub-gridded ADE-FDTD method, in which the overall time step size is no longer restricted by the CFL limit of the dense grid, is presented for simulating the 3-D GPR scenarios efficiently. Therefore, long simulation time due to small time step size is not required any more.

In conclusion, three contributions are made in this paper. First, a hybrid sub-gridded scheme, in which the implicit CN-FDTD is used in the local dense-grid region while the explicit FDTD is used in the global coarse-grid region,

is presented, and a time step size from the CFL limit of the coarse grid can be used throughout the computational region. Second, an efficient and stable implementation of exchanging data between the dense CN-FDTD region and coarse FDTD region is proposed, and no time-consuming temporal interpolation or extrapolation is necessary to synchronize the coarse and dense grids. Third, the DD technique is extended to the 3-D computational region that includes general dispersive, conductive and inhomogeneous media and fast calculation is achieved. Challenging computations, including the time-domain response from targets with high relative permittivity values, demonstrate that the proposed method is accurate and efficient for GPR numerical modeling. The proposed hybrid sub-gridded ADE-FDTD can also be applied to complex geometries and structures involving multiscale grid division, such as metamaterials, photonic crystals, microwave devices and antennas.

REFERENCES

[1] A. P. Annan, *Ground-Penetrating Radar in Near-Surface Geophysics: Society of Exploration Geophysicists*, D. K. Bulter, Ed. Tulsa, OK, USA: Soc. Exploration Geophysicists, 2005.

[2] H. M. Jol, *Ground Penetrating Radar Theory and Applications*. Amsterdam, The Netherlands: Elsevier, 2008.

[3] D. J. Daniels, "Surface-penetrating radar," *Electron. Commun. Eng. J.*, vol. 8, no. 4, pp. 165–182, Aug. 1996.

[4] K. Yee, "Numerical solution of initial boundary value problems involving Maxwell's equations in isotropic media," *IEEE Trans. Antennas Propag.*, vol. AP-14, no. 3, pp. 302–307, May 1966.

[5] A. Taflove and S. Hagness, *Computational Electrodynamics: The Finite-Difference Time-Domain Method*, 2nd ed. Boston, MA, USA: Artech House, 2000.

[6] H. X. Xu *et al.*, "Tunable microwave metasurfaces for high-performance operations: Dispersion compensation and dynamical switch," *Sci. Rep.*, vol. 6, Nov. 2016, Art. no. 38255.

[7] C. E. Fernandez-Rodriguez, A. A. Almeida De Salles, and D. L. Davis, "Dosimetric simulations of brain absorption of mobile phone radiation—The relationship between psSAR and age," *IEEE Access*, vol. 3, pp. 2425–2430, Dec. 2015.

[8] R. D. Morris, L. L. Morgan, and D. Davis, "Children absorb higher doses of radio frequency electromagnetic radiation from mobile phones than adults," *IEEE Access*, vol. 3, pp. 2379–2387, Dec. 2015.

[9] E. Moyroud *et al.*, "Disorder in convergent floral nanostructures enhances signaling to bees," *Nature*, vol. 550, pp. 469–474, Oct. 2017.

[10] D. Wu, X. Tang, K. Wang, and X. Li, "An analytical approach for optimal geometrical design of GaAs nanowires for maximal light harvesting in photovoltaic cells," *Sci. Rep.*, vol. 7, Apr. 2017, Art. no. 46504.

[11] M. Sarestoniemi, M. Hamalainen, and J. Iinatti, "An overview of the electromagnetic simulation—Based channel modeling techniques for wireless body area network applications," *IEEE Access*, vol. 5, pp. 10622–10632, Jun. 2017.

[12] Z. Jiang, S. Liu, and R. Malekian, "Analysis of a whole-space transient electromagnetic field in 2.5-dimensional FDTD geoelectric modeling," *IEEE Access*, vol. 5, pp. 18707–18714, Sep. 2017.

[13] J. M. Bourgeois and G. S. Smith, "A fully three-dimensional simulation of a ground-penetrating radar: FDTD theory compared with experiment," *IEEE Trans. Geosci. Remote Sens.*, vol. 34, no. 1, pp. 36–44, Jan. 1996.

[14] F. L. Teixeira, W. C. Chew, M. Straka, M. L. Oristaglio, and T. Wang, "Finite-difference time-domain simulation of ground penetrating radar on dispersive, inhomogeneous, and conductive soils," *IEEE Trans. Geosci. Remote Sens.*, vol. 36, no. 6, pp. 1928–1937, Nov. 1998.

[15] L. Gurel and U. Oguz, "Three-dimensional FDTD modeling of a ground-penetrating radar," *IEEE Trans. Geosci. Remote Sens.*, vol. 38, no. 4, pp. 1513–1521, Jul. 2000.

[16] A. Giannopoulos, "Modelling ground penetrating radar by GprMax," *Construction Building Mater.*, vol. 19, no. 10, pp. 755–762, Dec. 2005.

[17] S. Sardar and A. K. Mishra, "ASIN-based UWB radar for sludge monitoring," *IEEE Access*, vol. 2, pp. 290–300, 2014.

[18] L. Kulas and M. Mrozowski, "Low-reflection subgridding," *IEEE Trans. Microw. Theory Techn.*, vol. 53, no. 5, pp. 1587–1592, May 2005.

[19] K. Xiao, D. J. Pommerenke, and J. L. Drewniak, "A three-dimensional FDTD subgridding algorithm with separated temporal and spatial interfaces and related stability analysis," *IEEE Trans. Antennas Propag.*, vol. 55, no. 7, pp. 1981–1990, Jul. 2007.

[20] J. P. Berenger, "Extension of the FDTD huygens subgridding algorithm to two dimensions," *IEEE Trans. Antennas Propag.*, vol. 57, no. 12, pp. 3860–3867, Dec. 2009.

[21] B.-Z. Wang, Y. Wang, W. Yu, and R. Mittra, "A hybrid 2-D ADI-FDTD subgridding scheme for modeling on-chip interconnects," *IEEE Trans. Adv. Packag.*, vol. 24, no. 4, pp. 528–533, Nov. 2001.

[22] N. Diamanti and A. Giannopoulos, "Implementation of ADI-FDTD subgrids in ground penetrating radar FDTD models," *J. Appl. Geophys.*, vol. 67, no. 4, pp. 309–317, Apr. 2009.

[23] I. Ahmed and Z. Chen, "A hybrid ADI-FDTD subgridding scheme for efficient electromagnetic computation," *Int. J. Numer. Model. El.*, vol. 17, no. 3, pp. 237–249, Jun. 2004.

[24] X. Li, C. D. Sarris, and P. Triverio, "Structure-preserving reduction of finite-difference time-domain equations with controllable stability beyond the CFL limit," *IEEE Trans. Microw. Theory Techn.*, vol. 62, no. 12, pp. 3228–3238, Dec. 2014.

[25] C. Chang and C. D. Sarris, "A spatially filtered finite-difference time-domain scheme with controllable stability beyond the CFL limit: Theory and applications," *IEEE Trans. Microw. Theory Techn.*, vol. 61, no. 3, pp. 351–359, Jan. 2013.

[26] X. K. Wei, X. Zhang, N. Diamanti, W. Shao, and C. D. Sarris, "Sub-gridded FDTD modeling of ground penetrating radar scenarios beyond the Courant stability limit," *IEEE Trans. Geosci. Remote Sens.*, vol. 55, no. 12, pp. 7189–7198, Dec. 2017.

[27] G. Sun and C. W. Trueman, "Analysis and numerical experiments on the numerical dispersion of two-dimensional ADI-FDTD," *IEEE Antennas Wireless Propag. Lett.*, vol. 2, pp. 78–81, 2003.

[28] F. Zheng and Z. Chen, "Numerical dispersion analysis of the unconditionally stable 3-D ADI-FDTD method," *IEEE Trans. Microw. Theory Techn.*, vol. 49, no. 5, pp. 1006–1009, May 2001.

[29] G. Sun and C. W. Trueman, "Approximate Crank-Nicolson schemes for the 2-D finite-difference time-domain method for TE_z waves," *IEEE Trans. Antennas Propag.*, vol. 52, no. 11, pp. 2963–2972, Nov. 2004.

[30] S. Ogurtsov and G. Pan, "An updated review of general dispersion relation for conditionally and unconditionally stable FDTD algorithms," *IEEE Trans. Antennas Propag.*, vol. 56, no. 8, pp. 2572–2583, Aug. 2008.

[31] G. Sun and C. W. Trueman, "Accuracy of three unconditionally-stable FDTD schemes for solving Maxwell's equations," *Appl. Comput. Electromagn. Soc. J.*, vol. 18, no. 4, pp. 41–47, Nov. 2003.

[32] O. P. Gandhi, B.-Q. Gao, and J. Chen, "A frequency-dependent finite-difference time-domain formulation for general dispersive media," *IEEE Trans. Microw. Theory Techn.*, vol. 41, no. 4, pp. 658–665, Apr. 1993.

[33] R. J. Luebbers and F. Hunsberger, "FDTD for Nth-order dispersive media," *IEEE Trans. Antennas Propag.*, vol. 40, no. 11, pp. 1297–1301, Nov. 1992.

[34] J. A. Pereda, A. Vegas, and A. Prieto, "FDTD modeling of wave propagation in dispersive media by using the Mobius transformation technique," *IEEE Trans. Microw. Theory Techn.*, vol. 50, no. 7, pp. 1689–1695, Jul. 2002.

[35] M. Okoniewski, M. Mrozowski, and M. A. Stuchly, "Simple treatment of multi-term dispersion in FDTD," *IEEE Microw. Guided Wave Lett.*, vol. 7, no. 5, pp. 121–123, May 1997.

[36] S. D. Gedney, "An anisotropic perfectly matched layer-absorbing medium for the truncation of FDTD lattices," *IEEE Trans. Antennas Propag.*, vol. 44, no. 12, pp. 1630–1639, Dec. 1996.

[37] S. D. Gedney, "An anisotropic PML absorbing media for the FDTD simulation of fields in lossy and dispersive media," *Electromagnetics*, vol. 16, no. 4, pp. 399–415, Jul. 1996.

[38] X.-K. Wei, W. Shao, S.-B. Shi, Y.-F. Cheng, and B.-Z. Wang, "An optimized higher order PML in domain decomposition WLP-FDTD method for time reversal analysis," *IEEE Trans. Antennas Propag.*, vol. 64, no. 10, pp. 4374–4383, Oct. 2016.

[39] X. K. Wei, W. Shao, H. Ou, and B. Z. Wang, "Efficient WLP-FDTD with complex frequency-shifted PML for super-resolution analysis," *IEEE Antennas Wireless Propagat. Lett.*, vol. 16, pp. 1007–1010, 2017.

[40] X. K. Wei, W. Shao, and H. Ou, "Domain decomposition CN-FDTD method for analyzing dispersive metallic gratings," *IEEE Photon. J.*, vol. 9, no. 4, Aug. 2017, Art. no. 6101318.

[41] C. Chang, "A spatially-filtered finite-difference time-domain method with controllable stability beyond the Courant limit," M.S. thesis, Dept. Electron. Comput. Eng., Univ. Toronto, Toronto, ON, Canada, 2012.
[42] W. Yu and R. Mittra, "A conformal finite difference time domain technique for modeling curved dielectric surfaces," *IEEE Microw. Wireless Compon. Lett.*, vol. 11, no. 1, pp. 25–27, Jan. 2001.
[43] J. E. Hipp, "Soil electromagnetic parameters as functions of frequency, soil density, and soil moisture," *Proc. IEEE*, vol. 62, no. 1, pp. 98–103, Jan. 1974.
[44] F. J. Harris, "On the use of windows for harmonic analysis with the discrete Fourier transform," *Proc. IEEE*, vol. 66, no. 1, pp. 51–83, Jan. 1978.

XIAO-KUN WEI (S'16) was born in Tianshui, Gansu Province, China, in 1990. He received the B.S. degree in electronic information science and technology and the M.Sc. degree in electronics and communication engineering from the University of Electronic Science and Technology of China, Chengdu, China, in 2013 and 2015, respectively, where he is currently pursuing the Ph.D. degree in radio physics.

From 2016 to 2017, he was an International Visiting Graduate Student with the Department of Electrical and Computer Engineering, University of Toronto, Toronto, ON, Canada. His research interests include unconditionally stable and fast time-domain numerical methods and optimization techniques in electromagnetics.

WEI SHAO (M'13) was born in Chengdu, China, in 1975. He received the B.E. degree in electrical engineering and the M.Sc. and Ph.D. degrees in radio physics from the University of Electronic Science and Technology of China (UESTC) in 1998, 2004, and 2006, respectively.

He joined UESTC in 2007, where he is currently a Professor. From 2010 to 2011, he was a Visiting Scholar with the Electromagnetic Communication Laboratory, Pennsylvania State University, State College, PA, USA. From 2012 to 2013, he was a Visiting Scholar with the Department of Electrical and Electronic Engineering, The University of Hong Kong. His research interests include computational electromagnetics and antenna design.

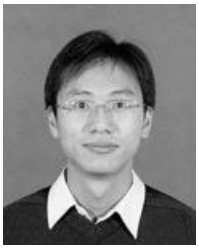

XIAO-HUA WANG (M'13) was born in Jiangsu Province, China, in 1980. He received the B.S. degree in electrical engineering and the M.S. and Ph.D. degrees in radio physics from the University of Electronic Science and Technology of China (UESTC), Chengdu, China, in 2002, 2005, and 2008, respectively.

From 2008 to 2009, he was an RF Research Engineer with Huawei Company, Shenzhen, China. From 2009 to 2010, he was with the Department of Electronic Engineering, City University of Hong Kong, Hong Kong, as a Research Staff. He is currently a Professor with UESTC. His research interests include computational electromagnetics, microwave passive circuits, and antenna design.